

1 Effect of groundwater forced seepage on heat 2 transfer characteristics of borehole heat 3 exchangers

4 Jiuchen Ma^{1,2,3}, Qian Jiang^{1,3*}, Qiuli Zhang^{1,3}, Yacheng Xie^{1,3}, Yahui Wang^{1,3}, Feiyu Yi^{1,3}

5
6 * Correspondence: 596797782@qq.com ¹ School of Energy Safety Engineering, Tianjin Chengjian
7 University, Tianjin 300384, China.

8 Full list of author information is available at the end of the article

9 **Abstract:** A borehole heat exchangers (BHEs) combined with pumping-injection well is
10 established in areas where groundwater is shallow but the seepage velocity is weak, which
11 sets up pumping and injection wells on both sides of the BHEs. According to the
12 three-dimensional unsteady state heat transfer model in aquifer, we derive the
13 convection-dispersion analytical solution of excess temperature in aquifer that considers
14 groundwater forced seepage and thermal dispersion effects in aquifer and the axial effect of
15 the BHEs. Then, we use dimensional analysis method and similarity criteria to build a
16 controllable forced seepage sandbox. The theoretical analysis is combined with the indoor
17 experiment test to verify the correctness and accuracy of the numerical simulation software
18 FEFLOW7.1. On this basis, we perform the numerical simulation calculation to explore the
19 effects of different pumping-injection flow volume on the Darcy flow velocity of the aquifer
20 where the BHEs are located, the average heat transfer efficiency and the heat transfer rates per
21 unit borehole depth of the BHEs. The results show that when the pumping flow volume is
22 increased from 200 m³·d⁻¹ to 1200 m³·d⁻¹, the Darcy velocity correspondingly increases to about
23 10 times the previous velocity. The average heat efficiency coefficient of the BHEs increases by
24 11.5% in cooling stage, and by 7.5% in heating stage. When the pumping-injection flow
25 volume is 400~600 m³·d⁻¹, the increment of heat transfer rates per unit borehole depth of the
26 BHEs reaches 12.8~17.9 W·m⁻¹ and 3.6~4.2 W·m⁻¹ during the cooling stage and heating stage
27 respectively, and then decreases as the flow volume increases gradually.

28 **Keywords:** borehole heat exchangers; groundwater forced seepage; analytical solution;
29 laboratory experiment; numerical simulation calculation; pumping-injection well
30

31 1. Introduction

32 Shallow geothermal resources in China are abundant but unevenly distributed. The
33 relevant documents clearly point out that the development and utilization of shallow
34 geothermal energy should follow the principle of adaption to local conditions (National
35 Development and Reform Commission 2017; China Geological Survey 2018). Ground source
36 heat pump (GSHP) system, as one of the main techniques of shallow geothermal production
37 (Beier 2014; Beier et al. 2011), should take full account of local conditions in the application
38 process. Moreover, borehole heat exchangers (BHEs) constitute a core part of the technology
39 and the magnitude of its heat exchange quantity directly affects the efficiency of the overall
40 unit. Therefore, it is particularly important to enhance heat transfer around the BHEs.

41 The heat transfer performance of the BHEs is studied usually by four methods, i.e.,
42 analytical method, numerical method, and in-situ thermal response test (TRT) and laboratory
43 test. In most related fields, one or two of the above methods are adopted commonly to study

44 the effect of groundwater natural seepage on the heat transfer performance of the BHEs
45 (Angelotti et al. 2014; Hu 2017; Choi et al. 2013; Wang et al. 2009).

46 Numerical simulations give accurate solutions that are conducive to theoretical analysis
47 but need extensive computational time. Hence, numerous numerical simulation softwares are
48 often applied to the research and design of the BHEs, but the correctness and accuracy of these
49 softwares should be verified before (Casasso and Sethi 2014; Cuan et al. 2017). Hecht-Méndez et al.
50 (2013) use FEFLOW, a finite element numerical simulation software, to perform the transient
51 heat transport simulations for the fifteen scenarios of 25 boreholes and study the distribution
52 of hydrodynamic field and temperature field in the homogeneous confined aquifer. Li et al.
53 (2018) analyze the effect of unsaturated soil properties and groundwater flow on the
54 performance of GSHP system by the simulation software COMSOL Multiphysics. The
55 numerical simulation is validated by combining experimental test results with the analytical
56 solution that takes the multiple-layer substrates and groundwater flow into consideration.

57 Analytical solutions are preferred in most practical applications because of their excellent
58 computational time and flexibility for parameterized design. The method of moving
59 heat-source is applied in most analytical solutions to solve the problem of heat transfer under
60 the impact of groundwater seepage (Li et al. 2015). Sutton and Nutter (2003) and Diao et al. (2004)
61 present an analytical solution considering groundwater flow. They both concluded that
62 groundwater flow could change considerably the temperature distribution in the vicinity of
63 the boreholes. Molina-Giraldo et al. (2011) evaluate the influence of thermal dispersion on
64 temperature plumes of geothermal systems by using analytical solutions. In the above
65 analytical solutions, the axial effect is not considered and the borehole is considered to be a
66 moving infinite line heat source. Molina-Giraldo et al. (2011) propose a moving finite line
67 source model (MFLS) which considers the combined effect of groundwater flow and axial
68 effects but does not take the influence of thermal dispersion into account. Groundwater
69 seepage affects heat transfer by involving gross heat convection and thermal dispersion, which
70 is significant for the long-term temperature response of the BHEs (Luo et al. 2016). Therefore, an
71 optimized analytical model, which considers the thermal dispersion effect in the MFLS model,
72 is proposed in this paper.

73 TRTs applied to some real environments that can truly reflect the heat transfer process of
74 BHEs under the specific regional climatic characteristics and hydrogeological conditions. Most
75 TRTs performed on a test borehole to estimate the thermo-physical properties and borehole
76 thermal resistance (Wang et al. 2009; Michopoulos et al. 2013; Choi and Ooka 2015). From the
77 viewpoint of model validation, the data from TRTs is not suitable because TRTs' test times are
78 short (usually 48-72 hours) and are susceptible to uncontrollable factors such as weather
79 conditions during testing (Li et al. 2015; Smith and Elmore 2018; Shirazi and Bernier 2014). The
80 indoor sandbox experiments enable to change some parameters, which is conducive to
81 improve the speed and test accuracy of the experiment (Zhang et al. 2016; Zhang et al. 2015)
82 because the experimental requirements have well controllability comparing with the TRT.

83 Most studies (Erol and François 2018; Samson et al. 2018; Hua et al. 2017; Zhang et al. 2014) point
84 out that the presence of groundwater significantly affects the heat transfer between BHE and
85 its surrounding aquifer. However, most of these study conclusions are obtained under the
86 condition of high natural seepage velocity, which is generally higher than $10^{-8} \text{ m}\cdot\text{s}^{-1}$. However,
87 many areas such as the Bohai Rim plain have abundant groundwater reserves but the natural
88 seepage velocity there is generally lower than $10^{-8} \text{ m}\cdot\text{s}^{-1}$. In this case, it is usually considered
89 that groundwater seepage has almost no effect on heat transfer of the BHEs. At this time, using
90 the traditional GSHP system would render groundwater idle without having the positive
91 effect that it should have. Therefore, it is necessary to optimize the traditional GSHP system
92 for this special hydrogeological condition.

93 For the long-term application of GSHP system, the cold and heat accumulation around
94 the BHEs and the heat transfer quantity of the BHEs decay year-by-year, domestic and foreign

95 scholars have proposed some optimized methods and improved measures to regulate heat
96 balance of the soil. Such as, solar assisted GSHP system (Østergaard et al. 2019; Nouri et al. 2019;
97 Biglarian et al. 2019), and cooling tower assisted GSHP system (Liu et al. 2018; Gong et al. 2018).
98 Nouri et al. (2019) and Liu et al. (2018) study solar assisted GSHP system and cooling tower
99 assisted GSHP system, respectively. Their research results show that the application of these
100 hybrid systems could be helpful to reach considerable savings of energy through using free
101 resources of stored heat in the ground and sun or air. However, solar-assisted GSHP system
102 and cooling tower assisted GSHP system occupy a large land area and are greatly affected by
103 seasonal and environmental factors.

104 Thus, based on the local special hydrogeological conditions and existing GSHP system in
105 Tianjin, China, this paper presents a BHEs combined with pumping-injection well: pumping
106 and injection wells are set on both sides of the BHEs. After reviewing other scholars'
107 researches on the heat transfer performance of the BHEs, we learn that most of them use one or
108 two methods including analytical methods, numerical methods, in-situ thermal response
109 testing (TRT) and laboratory tests to study the effect of groundwater natural seepage on the
110 heat transfer performance of the BHEs. So, we combine the theoretical analysis, the
111 experimental research, and the numerical simulation calculation to discuss the changing
112 trends of the Darcy flow velocity of aquifer, the dynamic changes of the average outlet water
113 temperature, average heat transfer efficiency of the BHEs. Based on this research, this paper
114 aims to explore the influence of the different pumping-injection flow volume on the heat
115 transfer characteristics of the BHEs under forced seepage. At the same time, it provides
116 research ideas for reducing soil thermal accumulation, alleviating soil thermal interference
117 and improving the heat transfer efficiency of the BHEs.

118 **2. Geological survey and underground thermo-physical properties**

119 2.1 Geological survey

120 China's Bohai Rim region includes the plains of the four provinces of Liaoning, Hebei,
121 Tianjin, Shandong and the surrounding mountainous areas (including the two peninsulas).
122 The Bohai Rim plain is formed in the middle Pleistocene (Q2) and the late Pleistocene (Q3) to
123 the Holocene (Q4) in the Quaternary period. The final formation of the Bohai Rim region is the
124 result of the accumulation of sediment caused by the accumulation of rivers (Rong et al.
125 2012).

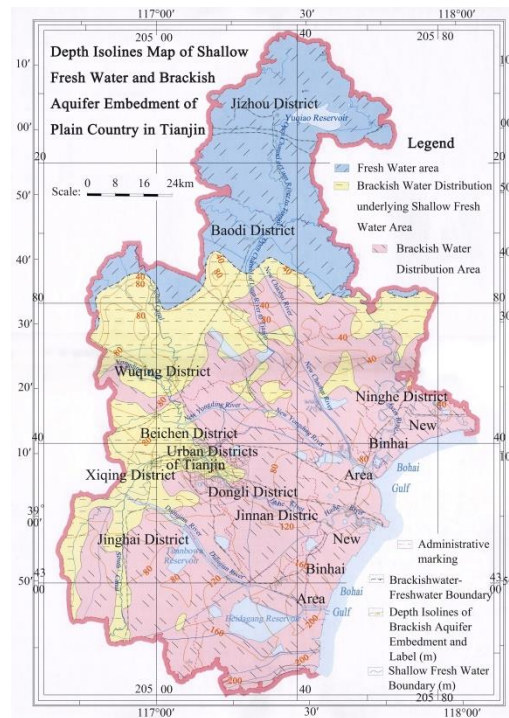


Figure 1. Depth Isolines Map of Shallow Aquifer Embedment of Plain Country in Tianjin, China

Tianjin is located in China's Bohai Rim plain, having abundant underground water and diverse hydrogeological structures. The whole Tianjin plain can be divided into the freshwater area, brackish water distribution underlying shallow freshwater area and brackish water area from north to south (Figure 1). In the structure of aquifer, the sandy layer transforms into medium coarse sand, medium sand, medium fine sand, fine sand and silty sand from north to south.

The distribution area of shallow underground brackish water in China's Binhai plain of Tianjin is 6,922 km², of which the brackish water area with a mineralization content of 2-3 g·L⁻¹ and 3-10 g·L⁻¹ are 3,753 km² and 3169 km² respectively, accounting for more than 2/3 of the city's total area (Zhou 2012). Groundwater resources are rich in reserves and convenient for exploitation, but the hydraulic gradient and the natural seepage generally range from 1.3×10⁻² m·a⁻¹ to 12×10⁻¹ m·a⁻¹. Therefore, a BHEs combined with pumping-injection well is suitable in Tianjin plain.

2.2 Underground thermo-physical properties

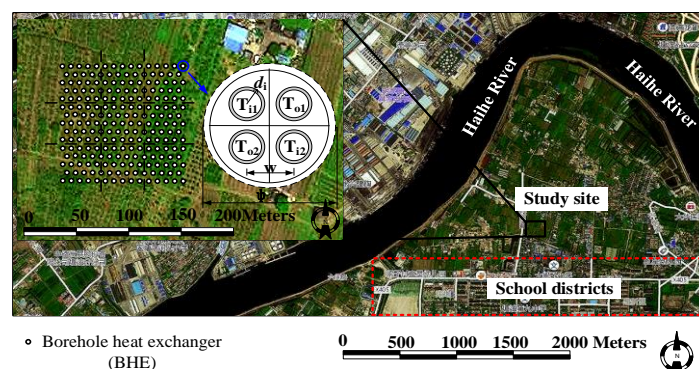


Figure 2. Location of study site in China, Tianjin, 2016 and plan view of the BHEs

The GSHP system that installed in Tianjin Binhai New Area, China, 2016 is taken as the project prototype (Figure 2). The project has a research area of 150×120 m² and a vertical depth of -83m that it is divided into 5 geotechnical layers. Among whole study area, the fine sand layer has stronger permeability that is regarded as a well-developed confined aquifer, which

148 interacts with silty sand layer to form shallow-groundwater accumulation section. The
 149 geotechnical distribution and physical parameters are shown in Table 1.
 150 **Table 1.** The physical parameters of the underground rock-soil layers

soil media	Depth of distribution σ (m)	horizontal permeability k_{XY} (m ²)	porosity ε_s	volumetric heat capacity of the soil $c_s \rho_s$ (J·m ⁻³ ·K ⁻¹)	thermal conductivity λ_s (W·m ⁻¹ ·K ⁻¹)	longitudinal thermal dispersivity α_L (m)	transverse thermal dispersivity α_T (m)	Initial temperature of soil layer $T_{so}/^\circ\text{C}$
clay	0-9	5.0·10 ⁻¹⁴	0.45	2.7·10 ⁶	1.10	0.3	0.03	16
silty clay	9-24	5.0·10 ⁻¹⁴	0.40	3.2·10 ⁶	1.20	0.3	0.03	16
fine sand	24-44	1.2·10 ⁻¹²	0.35	1.4·10 ⁶	0.95	3.0	0.30	16
silty sand	44-80	8.0·10 ⁻¹³	0.38	2.4·10 ⁶	1.60	0.1	0.01	16
silty clay	80-83	5.0·10 ⁻¹⁴	0.40	3.2·10 ⁶	1.20	0.3	0.03	16

151 The project, which is mainly responsible for the energy supply of the adjacent school,
 152 contains 219 BHEs with a center-to-center spacing of 4-5 m. The vertical depth of the borehole
 153 is 83 m and the 2U-DN32-HDPE-BHEs with the length of 80 m is arranged in the well. The
 154 expansive soil with sand is selected as the grout materials. Water is selected as the circulating
 155 refrigerant in the BHEs. The design parameters of the BHEs are shown in Table 2.

156 **Table 2.** Design Parameters of 2U-Type BHE

Parameter/Symbol (Unit)	Value
BHE depth /H (m)	80
borehole diameter / ψ (m)	0.13
outer diameter of branch pipe-in(out)/ $d_{i(o)}$ (m)	0.032
wall thickness of branch pipe-in(out)/ $b_{i(o)}$ (m)	0.0029
adjacent branch pipe distance / w (m)	0.05
thermal conductivity of pipe-in(out) material/ $\lambda_{pi(o)}$	0.60
thermal conductivity of refrigerant (water)/ λ_r	0.65
volumetric heat capacity of refrigerant (water) / $c_r \rho_r$	4.18·10 ⁶
volumetric heat capacity of grout/ $c_g \rho_g$ (J·(m ⁻³ ·K ⁻¹))	2.19·10 ⁶
thermal conductivity of grout/ λ_g (W·m ⁻¹ ·K ⁻¹)	1.90

157 3. Methods

158 3.1 Heat-seepage coupling model

159 It is assumed that the seepage process of aquifer satisfies the following conditions: the
 160 physical parameters of aquifer and groundwater do not change with temperature; the seepage
 161 direction of groundwater is single and the vertical seepage process is ignored. According to
 162 the continuity equation of seepage flow and Darcy law (Nam et al. 2008), the continuity
 163 governing equation (1) and momentum governing equation (2) in the anisotropic and
 164 homogeneous aquifers are established:

$$165 \quad [\varepsilon_s \gamma_f + (1 - \varepsilon_s) \gamma_s] \frac{\partial h}{\partial t} + \nabla \cdot u_f = Q_p \quad (1)$$

$$166 \quad u_f = - \frac{k \rho_f g}{\mu_f} \frac{\partial h}{\partial x} \quad (2)$$

167 In order to describe the change of heat transfer characteristics of the BHEs in the aquifer
 168 under complex space-time conditions accurately on the basis of the convective-conduction

169 equation (Capozza et al. 2013), the control equation of three-dimensional unsteady convective -
 170 thermal dispersion is established by taking the thermal dispersion effect into account.

$$171 \quad [\varepsilon_s \rho_f c_f + (1 - \varepsilon_s) \rho_s c_s] \frac{\partial T}{\partial t} = -\rho_f c_f u_f \nabla \cdot T + \nabla \cdot [(\Lambda^{\text{cond}} + \Lambda^{\text{disp}}) \nabla \cdot T] + Q_T \quad (3)$$

172 In which, the conductive part of thermodispersion tensor Λ^{cond} and the dispersive part of
 173 thermodispersion tensor Λ^{disp} are determined by equation (4) and (5) respectively.

$$174 \quad \Lambda^{\text{cond}} = [\varepsilon_s \lambda_f + (1 - \varepsilon_s) \lambda_s] \delta_{ij} \quad (4)$$

$$175 \quad \Lambda^{\text{disp}} = \rho_f c_f \left(\alpha_T u_f \delta_{ij} + (\alpha_L - \alpha_T) \frac{u_{fi} u_{fj}}{u_f} \right) \quad (5)$$

176 The problem for determining solution of seepage flow is associated with the problem of
 177 heat transfer by the momentum equation (2), so the heat-seepage coupling model is
 178 constructed in the aquifer. The discharge (suction) heat process of the borehole can be
 179 considered as the source (sink) term in the aquifer thermal migration model. Because the
 180 diameter of the vertical borehole is much smaller than its depth, in order to consider
 181 effectively the influence of groundwater seepage on the heat transfer of BHE, the heat transfer
 182 process of BHE is simplified to the heat transfer process of the moving finite line heat source in
 183 the semi-infinite medium.

184 On the basis of considering the thermal dispersion effect and the spatial position of BHE,
 185 the moving finite line heat source model (MFLS) (Michopoulos et al. 2013) is improved. Under
 186 the premise of constant heat flow volume per unit length of BHE, the optimized analytical
 187 model (Eq.6-7) is obtained by applying the method of images and the moving source theory.
 188 The optimized analytical model takes into account the heat convection, heat conduction and
 189 thermal dispersion effects in the process of groundwater seepage to determine the transient
 190 temperature in the aquifer caused by heat from the heat exchanger and is coupled with the
 191 internal heat transfer process of the borehole.

$$192 \quad \Delta T(x, y, z, t) = \frac{q}{2\pi \sqrt{\lambda_x \lambda_y}} \exp \left[\frac{\rho_f c_f u_f (x - x')}{2\lambda_x} \right] \left[\int_0^H f(x, y, z, t) dz - \int_{-H}^0 f(x, y, z, t) dz \right] \quad (6)$$

$$193 \quad f(x, y, z, t) = \frac{1}{4\sqrt{(x-x')^2 + (y-y')^2 + (z-z')^2}} \left[\exp \left(-\frac{\rho_f c_f u_f \sqrt{\frac{(x-x')^2}{\lambda_x \lambda_x} + \frac{(y-y')^2}{\lambda_x \lambda_y} + \frac{(z-z')^2}{\lambda_x \lambda_z}}}{2} \right) \operatorname{erfc} \left(\frac{\sqrt{\frac{(x-x')^2}{\lambda_x \lambda_x} + \frac{(y-y')^2}{\lambda_x \lambda_y} + \frac{(z-z')^2}{\lambda_x \lambda_z}} \rho_e c_e - \frac{\rho_f c_f u_f t}{\lambda_x}}{2\sqrt{\frac{\rho_e c_e t}{\lambda_x}}} \right) \right. \\ \left. + \exp \left(-\frac{\rho_f c_f u_f \sqrt{\frac{(x-x')^2}{\lambda_x \lambda_x} + \frac{(y-y')^2}{\lambda_x \lambda_y} + \frac{(z-z')^2}{\lambda_x \lambda_z}}}{2} \right) \operatorname{erfc} \left(\frac{\sqrt{\frac{(x-x')^2}{\lambda_x \lambda_x} + \frac{(y-y')^2}{\lambda_x \lambda_y} + \frac{(z-z')^2}{\lambda_x \lambda_z}} \rho_e c_e + \frac{\rho_f c_f u_f t}{\lambda_x}}{2\sqrt{\frac{\rho_e c_e t}{\lambda_x}}} \right) \right] \quad (7)$$

194
 195 In the analytic model, $\rho_e c_e$ is the volumetric heat capacity of the porous medium (Eq.8).
 196 When the thermal conductivity in the aquifers is the same in each direction, the thermal
 197 conductivity components of the Λ^{cond} are determined by equation (9). λ_x and λ_y is the effective
 198 longitudinal and transverse thermal conductivity coefficient, respectively, which are
 199 determined by Eq.10 and Eq.11. r is the distance to the source located on the z -axis at the $(x_0,$
 200 $y_0, z')$ coordinates (Eq.12).

$$202 \quad \rho_e c_e = \varepsilon_s \rho_f c_f + (1 - \varepsilon_s) \rho_s c_s \quad (8)$$

$$\lambda_x^{\text{cond}} = \lambda_y^{\text{cond}} = \lambda_z^{\text{cond}} = \lambda_e = \varepsilon_s \lambda_f + (1 - \varepsilon_s) \lambda_s \quad (9)$$

$$\lambda_x = \lambda_e + \alpha_L u_f \rho_f c_f \quad (10)$$

$$\lambda_y = \lambda_e + \alpha_T u_f \rho_f c_f \quad (11)$$

$$r = \sqrt{(x - x_0)^2 + (y - y_0)^2 + (z - z_0)^2} \quad (12)$$

When the thermal dispersion effect in the aquifer is ignored ($\lambda_x = \lambda_y = \lambda_e$), the excess temperature analysis model (Eq.6) and (Eq.7) can be simplified to Eq. 13 and Eq.14.

$$\Delta T(x, y, z, t) = \frac{q}{2\pi\lambda_e} \exp\left[\frac{\rho_f c_f u_f (x - x')}{2\lambda_e}\right] \left[\int_0^H f'(x, y, z, t) dz' - \int_{-H}^0 f'(x, y, z, t) dz' \right] \quad (13)$$

$$f'(x, y, z, t) = \exp\left(-\frac{\rho_f c_f u_f r}{2\lambda_e}\right) \operatorname{erfc}\left(\frac{r\rho_e c_e - \rho_f c_f u_f t}{2\sqrt{\rho_e c_e \lambda_e t}}\right) + \exp\left(\frac{\rho_f c_f u_f r}{2\lambda_e}\right) \operatorname{erfc}\left(\frac{r\rho_e c_e + \rho_f c_f u_f t}{2\sqrt{\rho_e c_e \lambda_e t}}\right) \quad (14)$$

3.2 Experimental System

In order to ensure the reasonable use of the limited laboratory indoor space, the fine sand layer, which was a typical hydrogeological medium in shallow the aquifer, with the area of 20×16m² and the buried depth of 24~44m in Figure 2 were selected as the engineering prototype for designing and building a complete laboratory experimental system. The engineering prototype contained 6 ordinals arranged BHEs with the tube pitch of 4m.

Design and Construction of Experimental system

The experimental system consists of a sandbox, a heating apparatus, a flow conditioning apparatus and a data-acquisition apparatus (Figure 3). Since the seepage and heat transfer processes in the seepage sandbox and the engineering prototype followed the same form of governing equations (Eq.1-3), the similitude relation ratio of basic design parameters was determined by dimensional analysis method according to the principle of similarity criteria (Li et al. 2015; Mao et al. 2006).

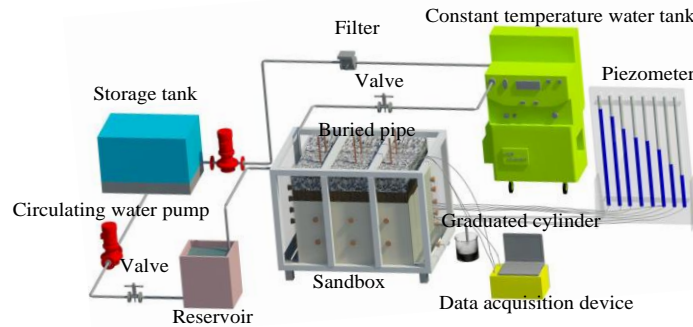


Figure 3. Schematic diagram of the experimental system

The proportional relationship between hydrogeology and thermophysical parameters of aquifers was 1:1 due to the use of equal volumetric weight filling of raw sand and seepage of raw water. In order to shorten the experimental period, the proportional relationship between the heat intensity of the BHEs and the difference of water head was set as 1:1. The geometric size proportional relationship between the actual and experimental was determined as 20:1. The Pr (Eq.15), Fo (Eq.16) and Pe (Eq.17) in the engineering prototype and the sandbox were required to be equal in order to ensure that the experimental system can reproduce effectively the heat-seepage migration process of the aquifer. Thus, the operation time proportional relationship between the actual and the experimental was determined to be 400:1 and the

235 seepage velocity proportional relationship between the actual and the experimental was
 236 determined to be 1:20, so as to determine other design parameters, as shown in Table 3.

$$237 \quad Pr = \frac{\rho_f \rho_e c_e}{\mu_f \lambda_e} = \frac{\rho_{fm} \rho_{em} c_{em}}{\mu_{fm} \lambda_{em}} = Pr_m \quad (15)$$

$$238 \quad Fo = \frac{\lambda_e t}{\rho_e c_e l^2} = \frac{\lambda_{em} t_m}{\rho_{em} c_{em} l_m^2} = Fo_m \quad (16)$$

$$239 \quad Pe = \frac{\rho_f c_f u l}{\lambda_e} = \frac{\rho_{fm} c_{fm} u_m l_m}{\lambda_{em}} = Pe_m \quad (17)$$

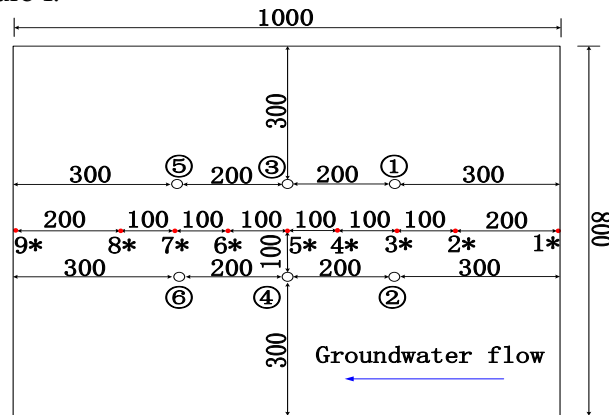
240
 241

Table 3. Engineering prototype and experimental system design parameters

classify	volume <i>x·y·z</i> (m ³)	pressure diaphragm thickness <i>σ</i> (m)	confined		heat transfer rates per unit borehole depth <i>q</i> (W · m ⁻¹)	Darcy velocity <i>u_t</i> (m · s ⁻¹)	operatio n time <i>t</i>
			aquifer (fine sand layer) thickness <i>σ_z</i> (m)	tube pitch <i>l</i> (m)			
prototype	20×16×20	4	12	4	50	1.2×10 ⁻⁷	90d
test-bed	1.0×0.8×1	0.2	0.6	0.2	50	2.4×10 ⁻⁶	5.4h

242 According to the geometric similarity ratio, we firstly set the sandbox to 1.2×0.8×1.2 m³
 243 while the seepage region was 1×0.8×1 m³ and the confined aquifuge region was 1×0.8×0.2 m³;
 244 the liquid supply/discharge region was 0.1 ×0.8 ×1.2 m³, which was symmetrically set at both
 245 ends. Then, we drill five overflow holes (Φ20 mm) with spacing of 0.2m in the centerline of
 246 plexiglas’s plate on the outsides of the liquid supply/discharge region. During the experiment,
 247 open the rubber plugs of overflow holes at different heights to control the hydraulic
 248 difference between the liquid supply/drainage region, so as to change the seepage velocity in
 249 the seepage region. In addition, the holes (Φ5 mm) of the plexiglass plate are evenly installed
 250 between liquid supply/discharge region and the seepage area, in order to ensure the seepage
 251 solution flows horizontally and evenly in the aquifer.

252 Select the K-type (±0.1°C) thermocouple that has been treated with waterproof and
 253 anti-corrosion treatment to measure the temperature of the aquifer. Nine K-type
 254 thermocouples are embedded at 0.5m from the bottom of the sandbox. Data acquisition
 255 equipment is used to record the temperature of the aquifer. Six PPR pipes with 1.5m-long,
 256 fixed on the bottom plate of the sandbox, are wound evenly with electric heating wire
 257 (50W/m) to simulate the BHEs. The plane layout of the BHEs and temperature observation
 258 points is shown as Figure 4.



○ ① ~ ⑥ Borehole heat exchanger (BHE)
 • 1* ~ 9* Temperature observation point

259
 260

Figure 4. Layout of the BHEs and temperature observation points (unit: mm)

261 Finally, select the precision bath circulator THD-3015 as the cold/heat source equipment,
 262 to ensure that the temperature of the circulating groundwater meets the requirements of the
 263 test. Furthermore, the outside of the sandbox device, connecting pipes, storage tank and
 264 reservoir are pasted with the thermal insulation materials with the thickness of 0.15 m. After
 265 that, fix respectively six K-type thermocouples on all six sides of the sandbox to measure the
 266 heat loss of the experimental system.

267 *Experimental scheme*

268 The sandbox is filled with equal volumetric weight by layered wet filling method, and
 269 each layer is 50mm thick raw sand layer. At the same time, the raw underground water is
 270 sprayed evenly and the sand layer is compacted, to ensure that the porous medium in the
 271 sandbox has unit weight of $1.68\pm 0.1 \text{ kg}\cdot\text{L}^{-1}$, which is similar to that of the underground aquifer.
 272 The raw sand is filled with a height of 1m, and then a 0.2m clay-gravel layer is laid on the
 273 upper part of the sandbox as a closed aquifer to isolate the aquifer from the external
 274 environment. The photograph of the sandbox without the thermal insulation material is
 275 shown as Figure 5.



276
 277 **Figure 5.** Photograph of the infiltration sandbox

278 After establishing experimental system, central air-conditioning keeps the room
 279 temperature at 18°C , and then inject the 16°C underground raw water into the sandbox for
 280 exhaust gas treatment of porous media. When all temperature observation points in the
 281 sandbox are maintained at $16\pm 0.1^{\circ}\text{C}$, and the water level in the piezometer is stable and no
 282 bubbles appeared, the porous medium of the sandbox can be considered as saturated aquifer.

283 Before starting experiment, it is proved that Darcy velocity was $2.4\pm 0.02\times 10^{-6} \text{ m}\cdot\text{s}^{-1}$ ($Pe\approx 2.5$)
 284 when the hydraulic difference is 0.2m, which satisfies the proportional relationship between
 285 actual and experimental seepage velocity 1:20. During the experiment, the 16°C underground
 286 raw water with 0.2m hydraulic difference is filled continuously into the sandbox to ensure a
 287 stable Darcy velocity, simultaneously, the BHEs ①~④ are opened in the test. The
 288 experimental run time is set at 5.4 h and the temperature of each observation point is
 289 recorded per 1 min. Through this experiment, it is found that the temperature measurement
 290 range of the six thermocouples outside the thermal insulation sandbox is $18\pm 0.5^{\circ}\text{C}$, so the heat
 291 loss from the sandbox is in negligible level.

292 **4. Results and Discussion**

293 4.1 Compared with analytical and experimental data

294 According to the engineering prototype, we use FEFLOW 7.1 to establish a geometric
 295 model, mesh division (triangular element non-equidistant) and set the parameters, and then
 296 perform the numerical simulation calculation. Meanwhile, we use MATLAB 2012 to calculate
 297 the transient temperature response caused by the running BHE in engineering prototype,

298 according to the unsteady analytical model of the excess temperature in the aquifer (Eq.6-7).
 299 Then, the experimental results and the analytical solutions of the engineering prototype are
 300 compared with the numerical solution of the engineering prototype.

301 In the numerical simulation calculation, the clay layer is defined as a confined aquifuge
 302 while the fine sand layer with a thickness of 20m exists as a confined aquifer. The clay layer in
 303 the upper part of the study area is defined as the impervious and adiabatic boundary while
 304 the external environmental impact is ignored. Moreover, the four flanks of the 20×16×83 m³
 305 model are defined as the fixed hydraulic head and constant temperature boundary. Then, the
 306 parameters of the six ordinals arranged BHEs in this area are set according to Table 2. In
 307 addition, the triangular element non-equidistant mesh generation is adopted in the entire
 308 geotechnical layer. The physical model has a total number of nodes of 51740 and a grid
 309 number of 93156. The fixed-time step method is used in the solution process. The total
 310 number of time steps is 324 when the time-step length is set to 1 min and the maximum
 311 iteration is 2500 times per step.

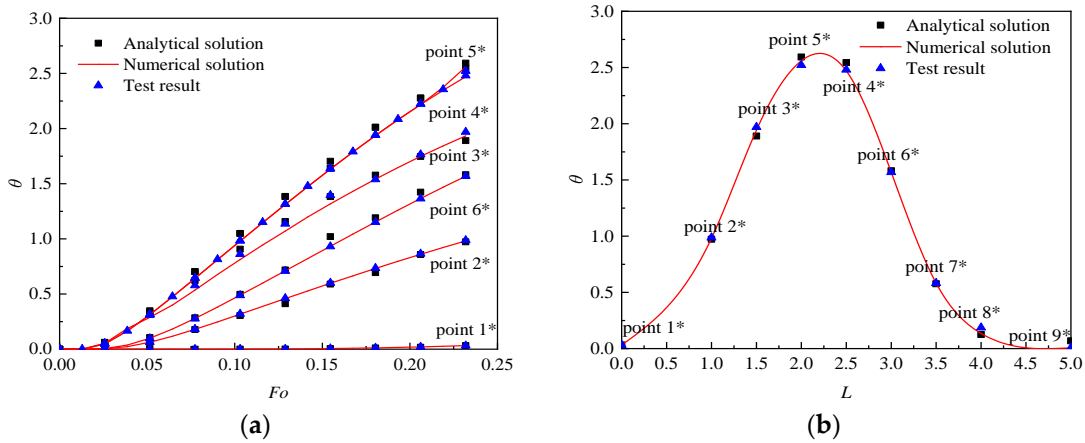
312 For facilitating the comparison, the time t , the excess temperature ΔT and the coordinate
 313 displacement x are all in a dimensionless form. Due to the different proportional relationship
 314 between the engineering prototype and the experimental system in operation time and
 315 geometric size, Fo is taken as dimensionless time (Eq.16), θ is taken as dimensionless excess
 316 temperature (Eq.18) and L is taken as dimensionless coordinate displacement (Eq.19).
 317 Meanwhile, the root mean square error (RMSE) of dimensionless excess temperature θ (Eq.20)
 318 is selected as the similarity index between experimental results, analytical solutions and
 319 numerical solutions.

320
$$\theta = \frac{4\pi\lambda_c\Delta T}{q} \tag{18}$$

321
$$L = \frac{x}{l} \tag{19}$$

322
$$RMSE = \sqrt{\frac{\sum_{i=1}^n (\theta_{N(i)/A(i)} - \theta_{E(i)})^2}{n}} \tag{20}$$

323 in which $\theta_{N(i)/A(i)}$ corresponds to the numerical solutions and analytical solutions respectively,
 324 and $\theta_{E(i)}$ corresponds to the experimental result.



325 **Figure 6.** Comparison of multi-tube (Four-tube) analytical solution and numerical solution with
 326 experimental result ($y=0m, z=0.5m$): (a) temperature response θ over Fo (the observation points 1*~6*); (b)
 327 temperature response θ over dimensionless distance L ($Fo=0.232$)

328 The RMSE between the analytical solutions and the experimental results in Figure 6(a)
 329 does not exceed 5% while the RMSE between the numerical solution and the experimental
 330 result does not exceed 1%. Besides, the RMSE between the analytical solution and the
 331 experimental result is 3.8% and the RMSE of the numerical solutions and experimental results
 332 is 0.5% in Figure 6(b). The results show that the analytical solution and experimental results

333 are consistent with the numerical solution, so FEFLOW 7.1 can simulate effectively and
 334 accurately the heat transfer process of the BHEs in the aquifer.

335 4.2 Compared with existing studied data

336 The numerical solutions regarding the mean temperature change of the aquifer are then
 337 compared to available data derived from (Hecht-Méndez et al. 2013). Since the studies in
 338 literature refer to different ground properties and groundwater velocities, as well as to
 339 different dimensions, the comparison is performed by calculating for each condition in the
 340 papers the Pe , Fo , $\bar{\theta}$.

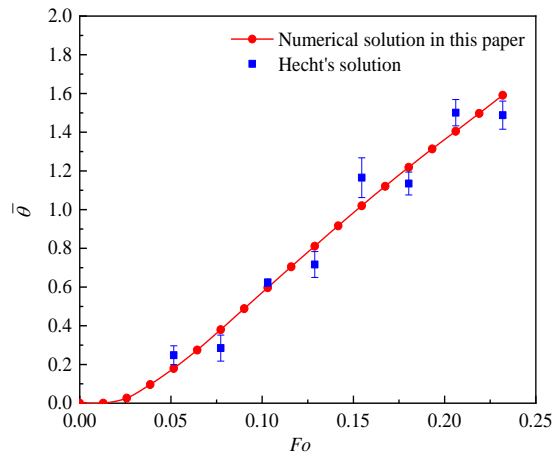


Figure 7. Comparison of multi-tube (Four-tube) numerical solution with Hecht's solution (Jozsef and Michael 2013): dimensionless mean temperature ($\bar{\theta} = 4\pi\lambda_e\Delta \bar{T}/q$) change over Fo

Table 4. Comparison between the numerical solutions and the Hecht's solution in: $\bar{\theta}$ and relative error for Fo

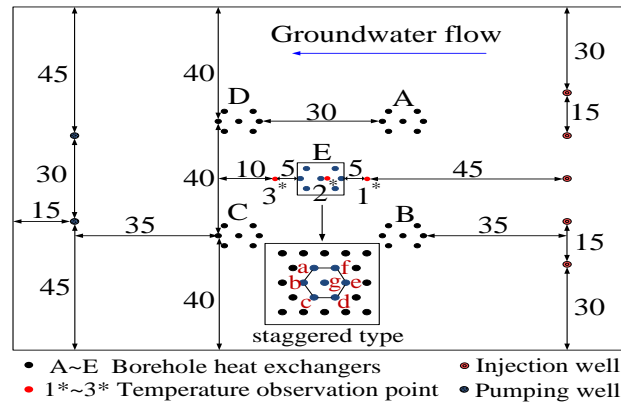
Fo	$\bar{\theta}$	Fit standard	$\bar{\theta}$ relative
		mean deviation	error (%)
0.05153	0.17937	0.248	4.9%
0.07729	0.37967	0.2846	-6.7%
0.10306	0.59666	0.62288	1.9%
0.12882	0.81075	0.7164	-6.7%
0.15459	1.01956	1.165	10.3%
0.18035	1.21858	1.1348	-5.9%
0.20612	1.40478	1.5009	6.8%
0.23188	1.59073	1.48792	-7.3%

341 After comparing Pe , it is found that the “scenario 12” in Hecht's research (Hecht-Méndez et
 342 al. 2013) are close to the working conditions in this paper (Figure 7). The results show that the
 343 maximum error is 10.3% and the other errors are less than 10%. Therefore, using FEFLOW7.1
 344 to simulate the heat transfer process of the BHEs under forced seepage is effective and
 345 correct.

346 5. Analysis of examples

347 This section explores the influence of the pumping-injection flow volume of the BHEs
 348 combined with pumping-injection well compared with the established traditional GSHP
 349 system on enhancing the heat transfer effect.

350 5.1 Generalized model and Operation scheme



351

352 **Figure 8.** Geometric arrangement of the BHEs and pumping - injection wells (unit: m)

353

354 Because of the complex and diverse layout of the on-site well group and a large number
 355 of boreholes, the BHEs (Figure 2) are generalized into five groups of the BHEs in Figure 8.
 356 For each group, there are seven boreholes arranged according to a staggered layout while the
 357 space between each borehole is 4~5 m. To ensure the groundwater synchronous recharge, two
 358 pumping wells and five injection wells are set up. Moreover, the design parameters of BHE
 359 are shown in Table 2. The seven working wells are all incomplete diving wells with a depth of
 60 m and a diameter of 0.4 m. Meanwhile, the filter is placed at a depth of 30~40 m.

360

361 On the grounds of the layout of the well group, the horizontal calculation area is 150×120
 362 m² and the vertical calculation range is 0~83 m. From the top to the bottom, the rock-soil
 363 layer with a thickness of 83 m is separated into five types of horizontal fault. The spatial
 distribution and physical properties of that layer are shown in Table 1.

364

365 In the numerical calculation, the silty clay layer in the upper and lower part of the study
 366 area is defined as the impervious and adiabatic boundary as the effects of atmospheric
 367 rainfall and evaporation are ignored. The four flanks of the physical model are defined as the
 368 fixed hydraulic head and constant temperature boundary. In addition, the pumping-injection
 369 wells are defined as the constant flow boundary. The triangular element non-equidistant
 370 mesh division is adopted for each rock-soil layer. Local refinement of the mesh is set in the
 location of the BHEs and the pumping-injection wells.

371

372 The number of total nodes and grid in the physical model is 248,752 and 413,295. The
 373 fixed-time step method is used in the solution process. The time step, the total time step and
 374 the maximum iteration are set to 1d, 3650 and 2500(times per step) respectively. Based on the
 375 established model, the numerical simulation calculation is carried out for eight kinds of
 operation modes respectively (Table 5).

376

Table 5. Operation scenarios of the coupling pumping-injection wells and the BHEs

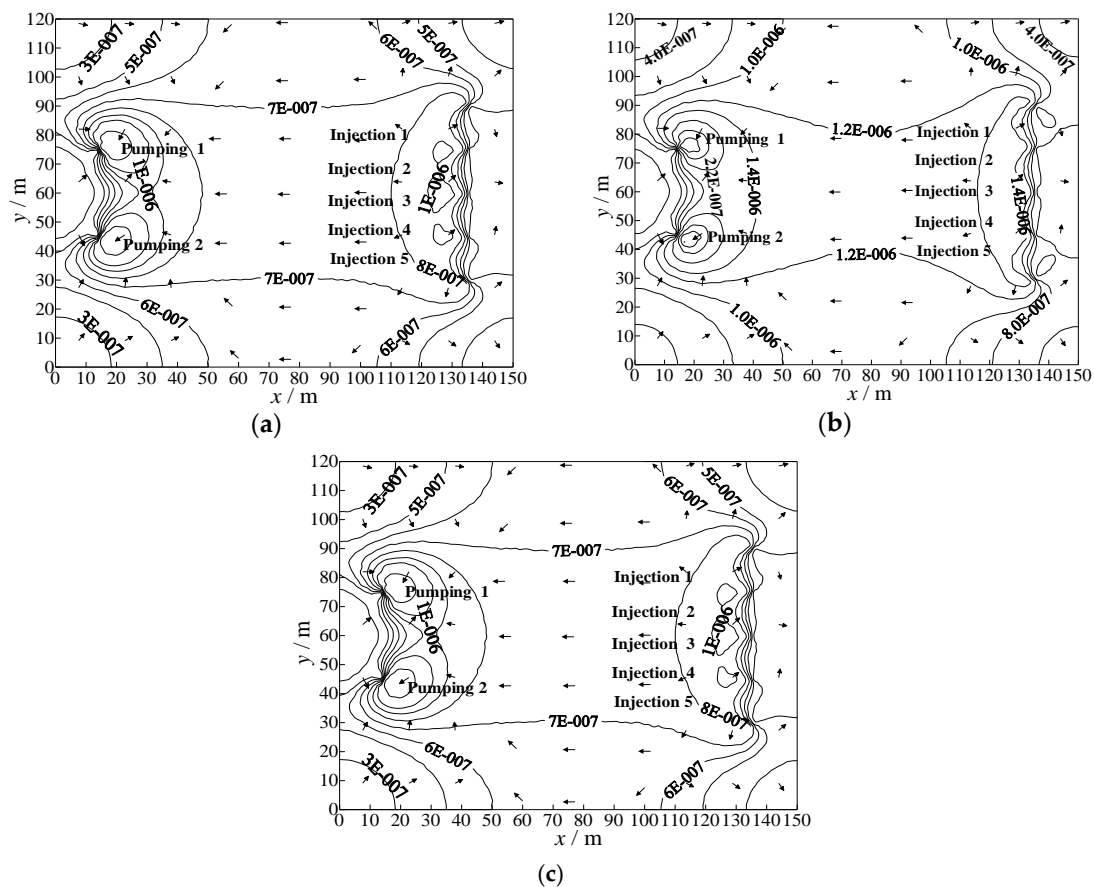
Scenario	Total flow volume of refrigerant per borehole (m ³ ·d ⁻¹)	Pumping quantity of single well (m ³ ·d ⁻¹)	Recharge quantity of single well (m ³ ·d ⁻¹)
1	30	0	0
2	30	100	40
3	30	200	80
4	30	300	120
5	30	400	160

6	30	500	200
7	30	600	240
8	30	700	280

377 To divide one operation cycle (1 year) into four stages that are followed by summer
 378 cooling stage (4 months), autumn intermittent stage 1 (2 months), winter heating stage (4
 379 months) and spring intermittent stage 2 (2 months). The system runs five operation cycles
 380 and the BHEs operate continuously for 10 hours per day in both the cooling and heating stage.
 381 Set the BHEs to non-constant power heat absorption (dissipation) operation. The inlet water
 382 temperature of the BHEs during cooling/heating stage is constant at 31°C/6°C respectively.
 383 The temperature of the outlet water of the BHEs and the temperature of the inlet and outlet
 384 water on the side of the heat pump unit change gradually with the operation of the system.

385 5.2 Analysis and discussion

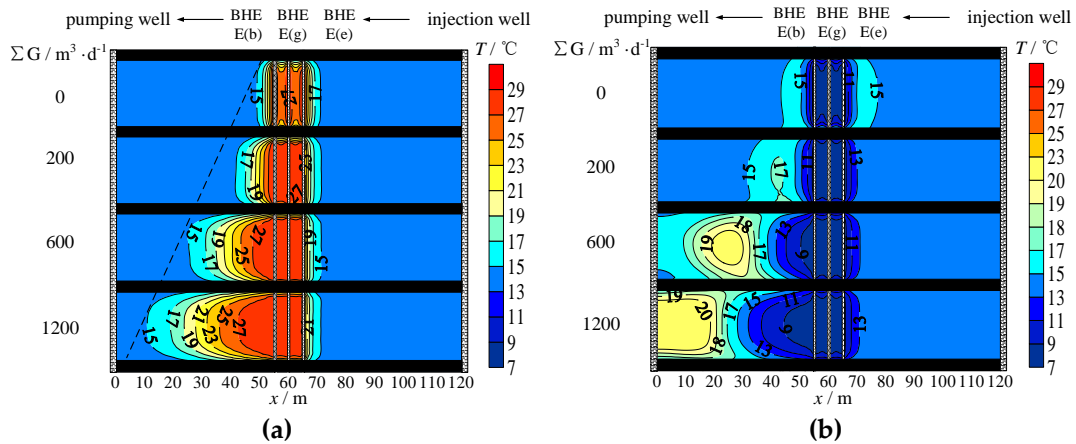
386 The Darcy velocity and the hydrodynamic distribution have a significant difference in
 387 the same aquifer since the total pumping-injection flow volume (ΣG) is different (Figure 9).
 388 Darcy velocity, which increases approximately 10 time, increases from $2.4 \sim 3.2 \times 10^{-7} \text{ m}\cdot\text{s}^{-1}$ to
 389 $2.0 \sim 3.0 \times 10^{-6} \text{ m}\cdot\text{s}^{-1}$ When the total pumping-injection flow volume increases from $200 \text{ m}^3\cdot\text{d}^{-1}$ to
 390 $1200 \text{ m}^3\cdot\text{d}^{-1}$.



391 **Figure 9.** Spatial hydrodynamic distribution in the fine sand layer on the 120d under the different total
 392 pumping-injection flow volume ΣG : (a) $\Sigma G=200 \text{ m}^3\cdot\text{d}^{-1}$; (b) $\Sigma G=600 \text{ m}^3\cdot\text{d}^{-1}$; (c) $\Sigma G=1200 \text{ m}^3\cdot\text{d}^{-1}$

393 Due to the difference of pumping-injection flow volume, profile temperature fields have
 394 a significant difference in the same aquifer (Figure 10). Taking the BHEs' well group E as the

395 research object, the injection well and the pumping well with a spacing of 120 m are defined
 396 as the upstream and downstream boundaries, respectively.



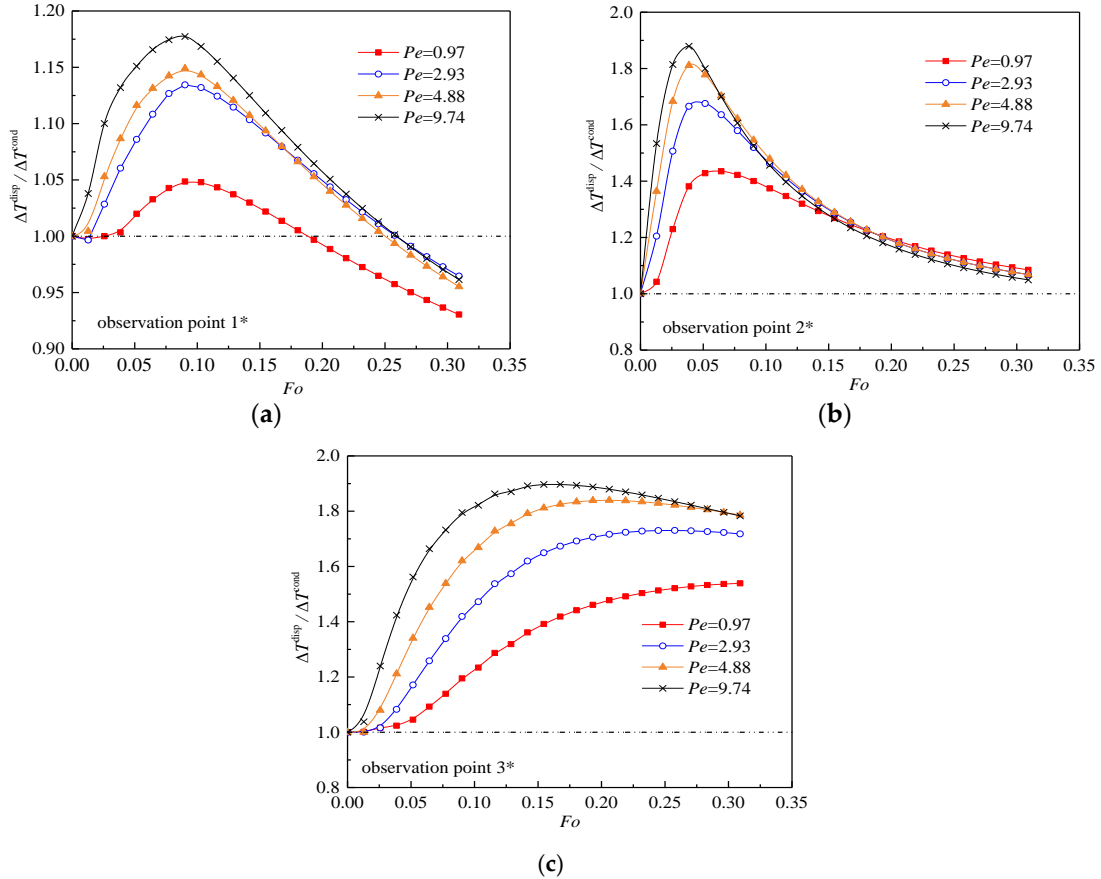
397 **Figure 10.** Profile temperature field in the fine sand aquifer under the different total pumping-injection
 398 flow volume: (a) the end of the cooling stage (120 d); (b) the end of the heating stage (300 d)

399 To describe accurately the evolution process of the aquifer's temperature field under
 400 different operation modes, the calculation area with a temperature change of $\pm 0.5\text{ }^{\circ}\text{C}$ is
 401 defined as the thermal diffusion range of the BHEs. Besides, the heat-influencing radius is
 402 defined as the coordinate distance between E (g) and the farthest acting position.

403 When the pumping-injection flow volume is $0\text{ m}^3\cdot\text{d}^{-1}$, there is only the heat conduction
 404 between the BHEs and the aquifer as well as between the aqueous medium units. The heat
 405 transfer process is slow and the heat influence range is diffused symmetrically around the
 406 BHEs. By the end of the cooling stage (120d), the thermal radius of the BHEs in both upstream
 407 and downstream areas is 11 m.

408 The range of thermal diffusion in the downstream area of the BHEs significantly expands
 409 with the pumping-injection flow volume increases from $200\text{ m}^3\cdot\text{d}^{-1}$ to $1200\text{ m}^3\cdot\text{d}^{-1}$. At the 120 d,
 410 the thermal radius along the direction of pumping reaches 19 m, 35 m and 49 m, so the
 411 thermal radius of $1200\text{ m}^3\cdot\text{d}^{-1}$ is 2.6 times of that of $200\text{ m}^3\cdot\text{d}^{-1}$. With the increase of the flow
 412 volume, the migration speed of the temperature fronts accelerates and the thermal radius
 413 enlarges continuously, moreover, the thermal radius in the upstream zone is smaller than
 414 11m.

415 According to the theory of heat and mass transfer, it is precisely because of the increase
 416 of Darcy velocity that the convective heat transfer intensity and thermomechanical dispersion
 417 effect are improved correspondingly, thereby expanding the range of thermal diffusion in the
 418 downstream region and alleviating the thermal accumulation phenomenon of BHE. So, in
 419 order to obtain the difference between the temperature response ΔT^{disp} with forced
 420 groundwater seepage and the temperature response ΔT^{cond} without groundwater seepage at
 421 different temperature observation points, the dynamic variation of $\Delta T^{\text{disp}}/\Delta T^{\text{cond}}$ with time is
 422 calculated (Figure 11).

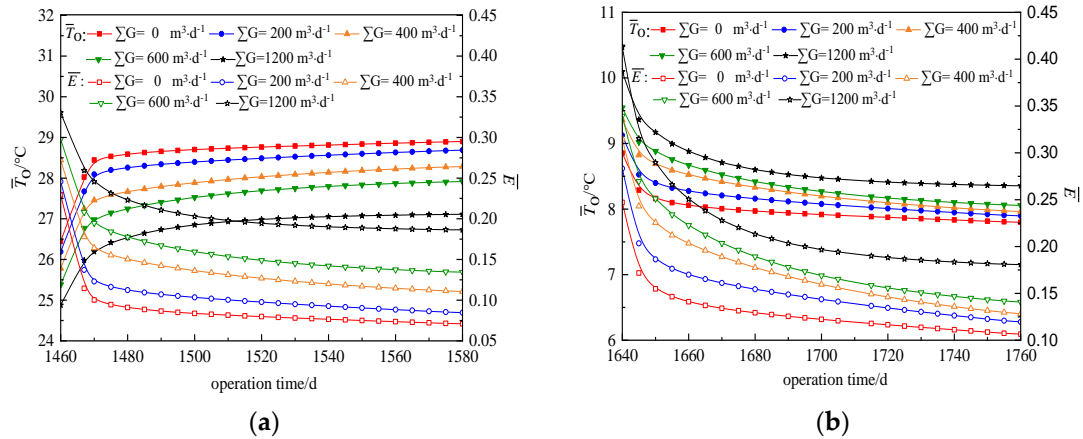


423 **Figure 11.** Temperature response dynamic curve in the fine sand aquifer at the first cooling stage: (a) the
 424 upstream area of the BHEs (the observation point 1*); (b) the inside area of the BHEs (the observation
 425 point 2*); (c) the downstream area of the BHEs (the observation point 3*)

426 As shown in Figure 11 (a), the mutative extent of temperature decreases gradually with the
 427 running time. When the running time exceeds 50% of the whole period ($Fo \geq 0.2$), $\Delta T^{\text{disp}}/\Delta T^{\text{cond}} < 1$. As
 428 shown in Figure 11 (b), $\Delta T^{\text{disp}}/\Delta T^{\text{cond}}$ tends to be stable gradually with time. At the end of the cooling
 429 stage (120d), $\Delta T^{\text{disp}}/\Delta T^{\text{cond}} > 1$. The change of Darcy velocity has no obvious influence on the change
 430 rate and amplitude of excess temperature because the thermal convection and thermal dispersion
 431 enhances thermal interference between the BHEs. As shown in Figure 11 (c), with the passage of time,
 432 the excess temperature tends to be stable and the curve of $\Delta T^{\text{disp}}/\Delta T^{\text{cond}}$ tends to be smooth. The
 433 mutative degree of excess temperature enhances with the increase of Darcy velocity but the difference
 434 between ΔT^{cond} and ΔT^{disp} tends to decrease when Darcy velocity increases to a certain extent.

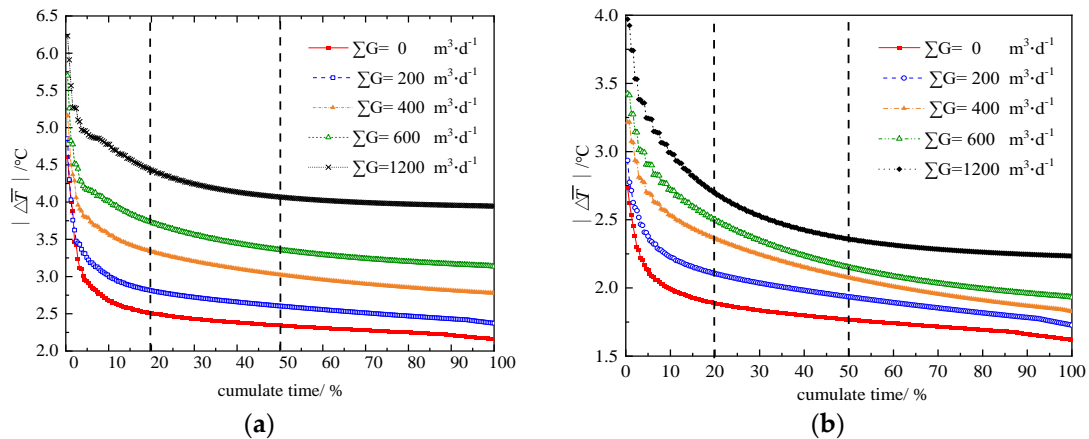
435 In this paper, the ratio of actual average heat exchange quantity (\bar{Q}) to theoretical
 436 average heat exchange quantity (\bar{Q}') of the BHEs is defined as the average heat transfer
 437 efficiency coefficient (\bar{E}), revealing the degree to which the BHEs performance deviates from
 438 the theoretical heat transfer under different operating conditions. At the early stage of various
 439 operation modes, due to the large temperature difference in heat transfer between the
 440 boreholes and the rock-soil layer, the temperature difference between the inlet with outlet
 441 water of the BHEs is higher and the corresponding energy efficiency coefficient also rise,
 442 (Figure 12). The heat exchange rate reduces because of the decreasing temperature difference
 443 between the boreholes and the surrounding medium. As a result, the temperature difference
 444 of the inlet and outlet water of the BHEs decreases rapidly. At the end of the fifth operation
 445 cycle, the average heat transfer efficiency of the five types of operation modes in the cooling

446 stage is 7.1%, 8.5%, 11.1%, 13.4% and 18.6% while the average heat transfer efficiency in the
 447 heating stage is 10.6%, 11.9%, 12.8%, 14.6% and 18.1% respectively.



448 **Figure 12.** Dynamic change of the average outlet water temperature (\bar{T}_o) and the average heat transfer
 449 efficiency ($\bar{E} = \bar{Q} / \bar{Q}' = |\bar{T}_i - \bar{T}_o| / |\bar{T}_i - \bar{T}_{so}|$) of the BHEs in the fifth operation cycle: (a) the cooling stage;
 450 (b) the heating stage

451 The cumulative distribution curve can be used as another evaluation index to describe
 452 the duration of a certain heat exchange efficiency of the BHEs (Figure 13). The cumulative
 453 distribution curve means that under cooling and heating stage, the absolute value of the
 454 water temperature difference between the inlet and outlet of the BHEs corresponding to the
 455 wellbore during the operation time is counted and arranged in descending order, and the
 456 temperature difference between the inlet and outlet of the BHEs is cumulatively time-varying
 457 distribution curve.



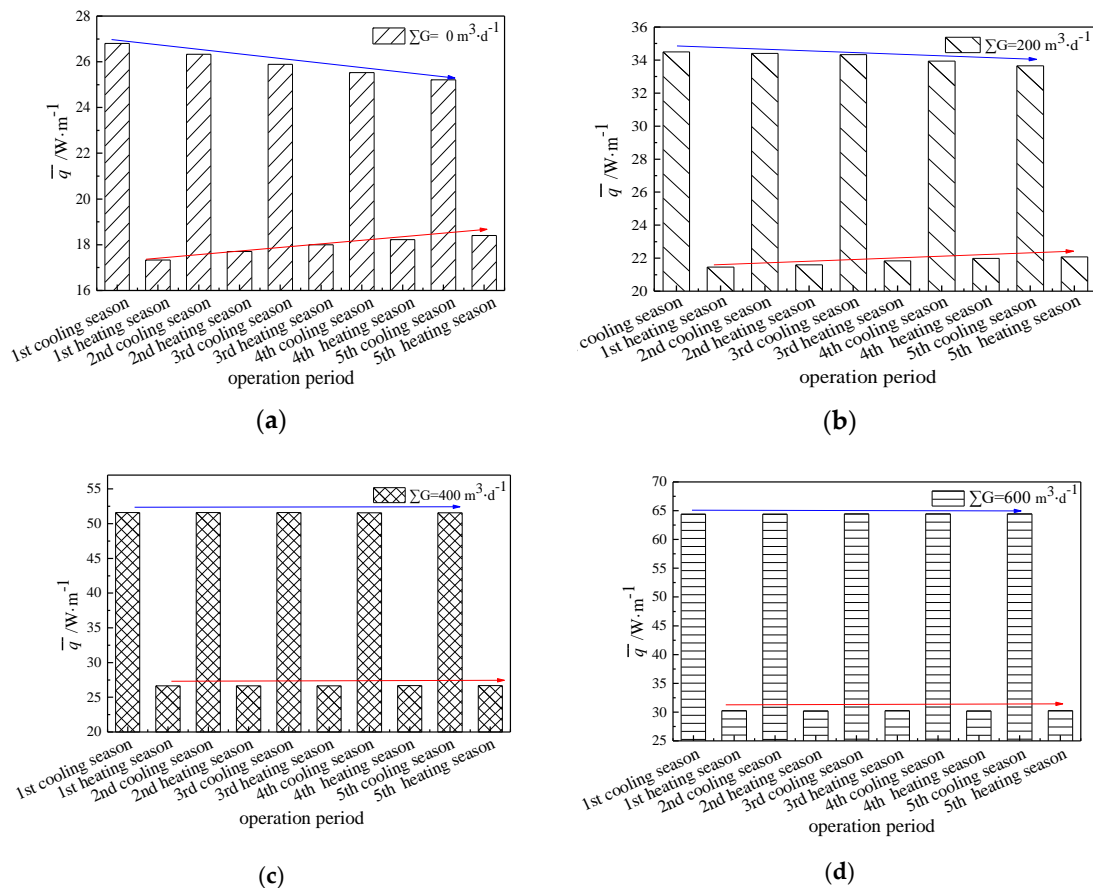
458 **Figure 13.** Cumulative distributions of the temperature difference of the inlet and outlet water of the
 459 BHEs: (a) the cooling stage; (b) the heating stage

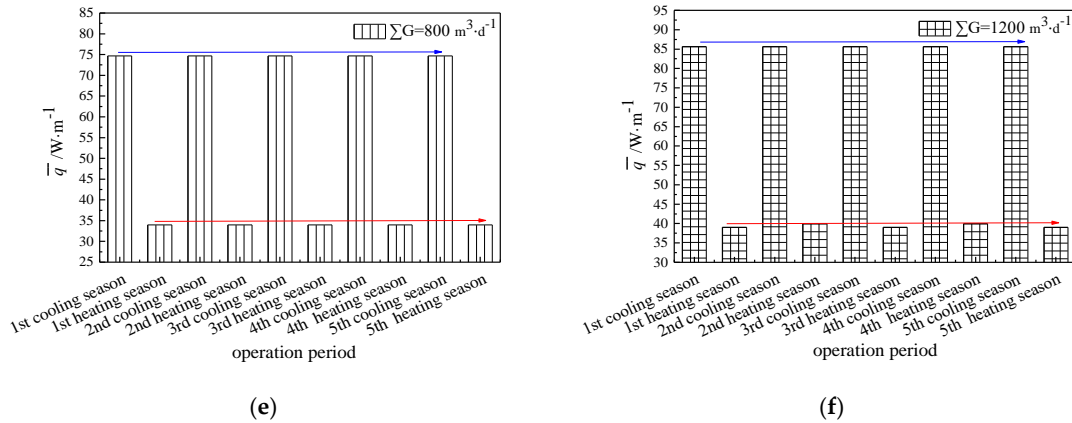
460 The absolute values of the inlet and outlet temperature difference of the BHEs is
 461 arranged in descending order, and the cumulative average temperature difference
 462 distribution in the cooling stages and heating stages over the whole simulation numerical
 463 stages (5 years) is calculated. When the cumulate time exceeds 20% of the total operation
 464 stage, the temperature difference tends to be moderate, when the cumulate time reaches 50%
 465 and the temperature difference reaches a steady state.

466 The inlet and outlet temperature difference of the BHEs corresponding to the median
 467 time is used as another evaluation index to compare the heat transfer performance of the
 468 BHEs under different modes. In cooling stage, the median of temperature difference is 2.34 °C

469 when the pumping-injection flow volume is $0 \text{ m}^3\cdot\text{d}^{-1}$. With the pumping-injection flow
 470 volume rises from $200 \text{ m}^3\cdot\text{d}^{-1}$ to $1200 \text{ m}^3\cdot\text{d}^{-1}$, the growth rate of the median temperature
 471 difference varies from 11.5% to 73.9%. In heating stage, the median temperature difference is
 472 1.76°C when the BHEs run individually. With the pumping-injection flow volume increases
 473 from $200 \text{ m}^3\cdot\text{d}^{-1}$ to $1200 \text{ m}^3\cdot\text{d}^{-1}$, the growth rate of the median temperature difference increases
 474 from 10.2% to 34.1%. As the pumping-injection flow volume, Darcy velocity and the heat
 475 exchange intensity of the BHEs all increase, thereby the decline rate of the temperature
 476 difference slows down while the time required reaching a steady state increase.

477 The heat transfer per unit depth of the BHEs (\bar{q}) is determined by the circulating water
 478 volume in the BHEs, the thickness of different rock and soil layers, and the temperature
 479 difference between the inlet and outlet water of the BHEs. Therefore, under different
 480 operating conditions, we use the \bar{q} as an evaluation parameter for the heat transfer
 481 characteristics of the BHEs in various rock and soil layers. The \bar{q} rise gradually when
 482 pumping and injection flow volume increases (Figure 14). Taking the fifth year as an example,
 483 the \bar{q} in cooling and heating stages with the increase of the pumping-injection flow volume
 484 from $0 \text{ m}^3\cdot\text{d}^{-1}$ to $1200 \text{ m}^3\cdot\text{d}^{-1}$ varies from $30.3 \text{ W}\cdot\text{m}^{-1}$ and $25.4 \text{ W}\cdot\text{m}^{-1}$ to $82.2 \text{ W}\cdot\text{m}^{-1}$ and 39.6
 485 $\text{W}\cdot\text{m}^{-1}$ respectively.

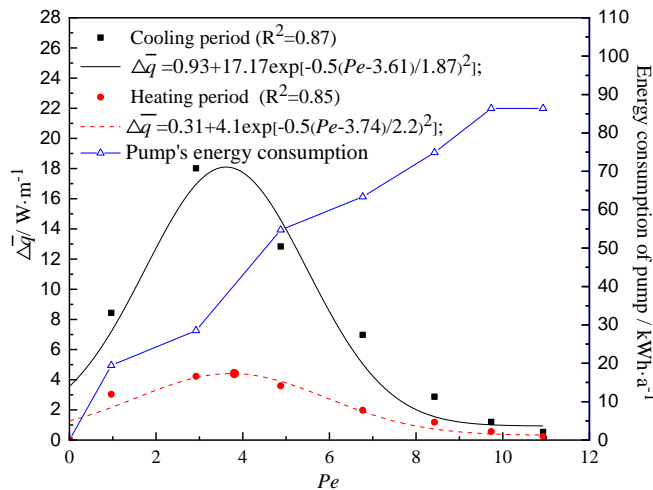




486 **Figure 14.** Average heat transfer rates per unit borehole depth of the BHEs ($\bar{q}=(\rho r c_r M \Delta \bar{T})/H$) in the fine
 487 sand layer over the whole operation period under different pumping-injection flow volume ΣG : (a)
 488 $\Sigma G=0 \text{ m}^3 \cdot \text{d}^{-1}$; (b) $\Sigma G=200 \text{ m}^3 \cdot \text{d}^{-1}$; (c) $\Sigma G=400 \text{ m}^3 \cdot \text{d}^{-1}$; (d) $\Sigma G=600 \text{ m}^3 \cdot \text{d}^{-1}$; (e) $\Sigma G=800 \text{ m}^3 \cdot \text{d}^{-1}$; (f) $\Sigma G=1200$
 489 $\text{m}^3 \cdot \text{d}^{-1}$

490 Thermal accumulation becomes serious with the continuous operation of the system,
 491 then the average heat transfer efficiency gets lower on the condition that the pumping and
 492 injection well ceases to work or the pumping-injection flow volume come to be smaller (200
 493 $\text{m}^3 \cdot \text{d}^{-1}$). As a result, cooling and heating quantity is declining every year. However, the
 494 rock-soil layer is not a single cold or heat source while an energy storage body has certain
 495 thermal storage and rejection. Therefore, thermal accumulation in the wells group’s area
 496 enhances the heat storage capacity of the rock-soil layer across the season in the summer.
 497 During the heating stage, the temperature of the rock-soil layer is higher than the initial stage.
 498 The temperature difference between the soil and the circulating solution increases so that the
 499 heat exchange quantity of the BHEs is improved at this stage.

500 Under the cooling and heating stages, the relation between $\Delta \bar{q}$ (known as the increment
 501 of average heat transfer rate per unit depth of BHEs) and Pe is determined by fitting which
 502 shows that $\Delta \bar{q}$ is distributed as a Gaussian function with the uptrend of Pe (Figure 15).
 503 Although the effect of convective heat transfer and thermal dispersion between the BHEs and
 504 the rock-soil layer can be enhanced effectively by strengthening the velocity of groundwater
 505 seepage, the average heat transfer rates per unit borehole depth of the BHEs \bar{q} does not raise
 506 linearly with the increase of the pumping-injection flow volume.



508 **Figure 15.** The total energy consumption of pumps and the increment of heat transfer rate per unit
 509 depth of the BHEs ($\Delta \bar{q} = \bar{q}_{t+1} - \bar{q}_t$) change over Pe

510 The research shows that Darcy velocity is only $0.6 \times 10^{-6} \sim 1.4 \times 10^{-6} \text{ m} \cdot \text{s}^{-1}$ when the pumping
 511 and injection flow volume is $400 \sim 600 \text{ m}^3 \cdot \text{d}^{-1}$, but the $\Delta \bar{q}$ respectively reaches $12.8 \sim 17.9 \text{ W} \cdot \text{m}^{-1}$
 512 and $3.6 \sim 4.2 \text{ W} \cdot \text{m}^{-1}$ during the cooling stage and heating stage which are located on both sides
 513 of the extremum point of the distribution curve. As the designed Pumping-injection flow
 514 volume further increases, not only the $\Delta \bar{q}$ decreases gradually, but also the energy
 515 consumption of pumping and injection pumps increase that leads to the increase of operation
 516 cost of the system. Furthermore, the change of aquifer spatial structure will be irreversible if
 517 the forced seepage velocity is too high. Therefore, in order to obtain the best heat transfer
 518 enhancement effect, system environment and economic benefits, the pumping-injection flow
 519 volume when Darcy velocity reaches $0.6 \times 10^{-6} \sim 1.4 \times 10^{-6} \text{ m} \cdot \text{s}^{-1}$ is taken as the best reference range
 520 for the BHEs combined with pumping-injection well, so the best flow volume range of
 521 pumping-injection wells is $400 \sim 600 \text{ m}^3 \cdot \text{d}^{-1}$ in this paper.

522 6. Conclusion

523 In this article, we present a BHEs combined with pumping-injection well. Based upon the
 524 three-dimensional unsteady state heat transfer model in aquifer, we derive a
 525 convection-dispersion analytical solution of excess temperature in aquifer that considers
 526 groundwater forced seepage and thermal dispersion effects in aquifer and the axial effect of
 527 the BHEs. At the same time, according to the dimensional analysis method and the similarity
 528 criteria, we establish a forced seepage indoor 3-D sandbox. Then, we use the numerical
 529 simulation software FEFLOW7.1 to discuss how different pumping-injection flow volume
 530 affect the heat transfer characteristics of the BHEs. The main conclusions of this study can be
 531 summarized as follows:

532 (a) Based on the established mathematical model, we build an indoor sandbox and
 533 develop an analytical solution. According to the engineering prototype, we use FEFLOW 7.1
 534 to establish a geometric model for the numerical simulation calculation. The results indicate,
 535 the analytical solution and experimental results are roughly consistent with the numerical
 536 solution: the RMSE between the analytical result and the experimental result is 3.8%; the
 537 RMSE of the numerical result and experimental results is 0.5%. Thus, the numerical
 538 simulation software FEFLOW7.1 can simulate effectively and correctly the evolution process
 539 of the aquifer temperature field during the taking heat of the BHEs.

540 (b) When the pumping-injection flow volume increases from $200 \text{ m}^3 \cdot \text{d}^{-1}$ to $1200 \text{ m}^3 \cdot \text{d}^{-1}$,
 541 Darcy velocity in the fine sand layer increases from $2.4 \sim 3.2 \times 10^{-7} \text{ m} \cdot \text{s}^{-1}$ to $2.0 \sim 3.0 \times 10^{-6} \text{ m} \cdot \text{s}^{-1}$ and
 542 the effect of convective heat transfer and thermal dispersion is intensified. In the downstream
 543 region of the BHEs, the thermal action radius is 2.6 times of the original radius. Hence, the
 544 BHEs combined with pumping-injection well can reduce soil thermal accumulation and
 545 alleviate soil thermal interference effectively.

546 (c) For long-term running the BHEs, the cumulative distribution curve of the inlet and
 547 outlet water average temperature difference is introduced to describe the duration of a certain
 548 heat exchange efficiency of the BHEs. The average temperature difference corresponding to
 549 the median time is used as a new parameter for evaluating the heat transfer performance of
 550 BHEs. In cooling stage, the pumping-injection flow volume rises from $200 \text{ m}^3 \cdot \text{d}^{-1}$ to $1200 \text{ m}^3 \cdot \text{d}^{-1}$,

551 the growth rate of the median temperature difference varies 62.4%. In heating stage, the
 552 pumping-injection flow volume increases from 200 m³·d⁻¹ to 1200 m³·d⁻¹, the growth rate of
 553 the median temperature difference increases 23.9%. At the same time, the average energy
 554 efficiency coefficient of the BHEs improves 11.5% (cooling stage) and 7.5% (heating stage).

555 (d) The simulated calculation indicates that in cooling and heating stages, the heat
 556 transfer characteristic of the BHEs increases significantly with the increase of the Darcy
 557 velocity. However, the relation curve between the $\Delta \bar{q}$ and Pe has a Gaussian function
 558 distribution in cooling and heating stages. Therefore, the heat exchange quantity of the BHEs
 559 cannot be increased continuously by increasing the pumping-injection flow volume infinitely.
 560 The pumping-injection flow volume that can make Darcy velocity reaches $0.6 \times 10^{-6} \sim 1.4 \times 10^{-6}$
 561 m·s⁻¹ is the best reference range of the BHEs combined with pumping-injection well.

562 (e) The point of this paper is on the heat transfer characteristics of the BHEs. The default
 563 geographic parameters are the homogeneous of the same aquifer and the thickness is 20m.
 564 We all know that the greater the thickness of the aquifer, the better the heat transfer
 565 characteristics of the BHEs, but the influence of the thickness of the aquifer on the heat
 566 transfer characteristics of the BHEs is not the focus of this article. Later, we will study the
 567 influence of aquifer thermophysical properties (thermal conductivity, porosity, permeability,
 568 etc.) and heterogeneity on the heat transfer characteristics of the BHEs.

569 7. Declarations

570 **Author contributions:** JM and QJ performed conceptualization; JM and QJ performed data curation; JM
 571 and QJ performed formal analysis; JM and QJ provided methodology; QZ provided resources; YX and
 572 YW provided software simulation; FY validated data; QJ writted the original draft; JM and QJ improved
 573 and revised the manuscript. All authors read and approved the final manuscript.

574 **Funding:** This research was funded by National Natural Science Foundation of China of Funder, grant
 575 number 41402228; This research was funded by Enterprise science and technology commissioner project
 576 of Tianjin of Funder, grant number 19JCTPJ48100.

577 **Availability of data and materials:** The datasets generated and analyzed during the current study are
 578 available from the corresponding author on reason-able request.

579 **Acknowledgments:** Thanks to the Tianjin Institute of Geotechnical Investigation Surveying for the
 580 hydrogeological parameters and relevant data provided.

581 **Conflicts of Interest:** The authors declare that they have no competing interests.

582 **Author details:** ¹ School of Energy Safety Engineering, Tianjin Chengjian University, Tianjin 300384,
 583 China. ² Key Laboratory for Efficient Use of Low and Medium Grade Energy, Ministry of Education of
 584 China, Tianjin University, Tianjin 30072. ³ Research Center for Efficient Utilization Technology of
 585 Geothermal Energy, Tianjin Chengjian University, Tianjin 300384, China.

586 **Received: date** **Accepted: date**

587 **Published: date**

588

589 References

- 590 Angelotti A, Alberti L, Licata IL, et al. Energy Performance and Thermal Impact of a Borehole Heat
 591 Exchanger in a sandy aquifer: Influence of the groundwater velocity. *Energy Conversion and*
 592 *Management*. 2014; 77: 700-708.
- 593 Beier RA. Transient Heat Transfer in a U-tube Borehole Heat Exchanger. *Applied Thermal Engineering*.

- 594 2014; 62: 256-266.
- 595 Beier RA, Smith MD, Spitler JD. Reference Data Sets for Vertical Borehole Ground Heat Exchanger
596 Models and Thermal Response Test Analysis. *Geothermics*. 2011; 40: 79-85.
- 597 Biglarian H, Saidi MH, Abbaspour M. Economic and Environmental Assessment of a Solar-assisted
598 Ground Source Heat Pump System in a Heating-dominated Climate. *Environmental Science and
599 Technology*. 2019; 16: 3091-3098.
- 600 China Geological Survey. China Geothermal Energy Development Report. Beijing, China Petrochemical
601 Press: Beijing, China. 2018; pp.5-10. (in Chinese)
- 602 Choi JC, Park J, Lee SR. Numerical Evaluation of the Effects of Groundwater Flow on Borehole Heat
603 Exchanger Arrays. *Renewable Energy*. 2013, 52: 230-240.
- 604 Casasso A, Sethi R. Efficiency of Closed Loop Geothermal Heat Pumps: A Sensitivity Analysis.
605 *Renewable Energy*. 2014; 62: 737-746.
- 606 Cuan Y, Zhao X. 3D Dynamic Numerical Programming and Calculation of Vertical Buried Tube Heat
607 Exchanger Performance of Ground-Source Heat Pumps under Coupled Heat Transfer Inside and
608 Outside of Tube. *Energy and Buildings*. 2017; 139: 186-196.
- 609 Choi WJ, Ooka R. Interpretation of Disturbed Data in Thermal Response Tests Using the Infinite Line
610 Source Model and Numerical Parameter estimation method. *Applied Energy*. 2015; 148: 476-488.
- 611 Capozza A, Carli MD, Zarrella A. Investigations on the influence of aquifers on the ground temperature
612 in ground-source heat pump operation. *Applied Energy*. 2013; 107: 35.
- 613 Diao N, Li Q, Fang Z-H. Heat Transfer in Ground Heat Exchangers with Groundwater Advection.
614 *Thermal Sciences*. 2004; 43: 1203-1211.
- 615 Erol S, François B. Multilayer Analytical Model for Vertical Ground Heat Exchanger with Groundwater
616 Flow. *Geothermics*. 2018; 71: 294-305.
- 617 Gong X, Xia L, Ma Z, et al. Investigation on the Optimal Cooling Tower Input Capacity of a Cooling
618 Tower Assisted Ground Source Heat Pump System. *Energy and Buildings*. 2018; 174: 239-253.
- 619 Hu J. An Improved Analytical Model for Vertical Borehole Ground Heat Exchanger with Multiple-Layer
620 Substrates and Groundwater Flow. *Applied Energy*. 2017; 202: 537-549.
- 621 Hecht-Méndez J, Paly MD, Beck M, et al. Optimization of Energy Extraction for Vertical Closed-Loop
622 Geothermal Systems Considering Groundwater Flow. *Energy Conversion and Management*. 2013;
623 66: 1-10.
- 624 Hua J, Li G, Zhao X, et al. The Hot Stack Performance of the Shallow Geothermal Heat Pump System
625 with/without Intensification State of Groundwater Seepage in Nanjing (China). *Energy and
626 Buildings*. 2017; 150: 558-566.
- 627 Li C, Cleall JP, Mao J, et al. Numerical Simulation of Ground Source Heat Pump Systems Considering
628 Unsaturated Soil Properties and Groundwater Flow Applied. *Thermal Engineering*. 2018; 139:
629 307-316.
- 630 Li M, et al. Review of Analytical Models for Heat Transfer by Vertical Ground Heat Exchangers (GHEs):
631 A Perspective of Time and Space Scales. *Applied Energy*. 2015; 151: 178-191.
- 632 Luo J, Rohn J, Xiang W, et al. Review of Ground Investigations for Ground Source Heat Pump (GSHP)
633 Systems. *Energy and Buildings*. 2016; 117: 160-175.
- 634 Liu Z, Li Y, Xu W, et al. Performance and Feasibility Study of Hybrid Ground Source Heat Pump
635 System Assisted with Cooling Tower for one Office Building Based on one Shanghai Case. *Energy
636 Conversion and Management*. 2018; 173: 28-37.
- 637 Molina-Giraldo N, Bayer P, Blum P. Evaluating the Influence of Thermal Dispersion on Temperature
638 Plumes from Geothermal Systems Using Analytical Solutions. *Thermal Sciences*. 2011; 50:

- 639 1223-1231.
- 640 Molina-Giraldo N, Blum P, Zhu K, et al. A Moving Finite Line Source Model to Simulate Borehole Heat
641 Exchangers with Groundwater Advection. *Thermal Sciences*. 2011; 50: 2506-2513.
- 642 Michopoulos A, Zachariadis T, Kyriakis N. Operation Characteristics and Experience of a Ground
643 Source Heat Pump System with a Vertical Ground Heat Exchanger. *Energy*. 2013; 51: 349-357.
- 644 Mao X, Prommer H, Barry DA, et al. Three-dimensional Model for Multi-component Reactive Transport
645 with Variable Density Groundwater flow. *Environmental Modelling & Software*. 2006; 21: 615-628.
- 646 National Development and Reform Commission. The 13th Five-Year Plan for the Exploitation and
647 Utilization of Geothermal Energy. N.D.R.C. Publishing; Beijing, China, 2017. Available online:
648 http://www.ndrc.gov.cn/zcfb/zcfbtz/201702/t20170204_837203.html.(in Chinese)
- 649 Nam YJ, Ooka R, Hwang S. Development of a numerical model to predict heat exchange rates for a
650 ground-source heat pump system. *Energy and Buildings*. 2008; 40: 2133–2140.
- 651 Nouri G, Noorollahi Y, Yousefi H. Designing and Optimization of Solar Assisted Ground Source Heat
652 Pump System to Supply Heating, Cooling and Hot Water Demands. *Geothermics*. 2019; 82:
653 212–231.
- 654 Rong M, Shi J, Liu J. Dealing with the spatial synthetic heterogeneity of aquifers in the north china plain:
655 A case study of Luancheng County in Hebei Province. Doctoral Dissertation. Chinese Academy of
656 Geological Sciences. Beijing, China, 2012. (in Chinese)
- 657 Sutton MG, Nutter DW. A Ground Resistance for Vertical Bore Heat Exchangers with Groundwater
658 Flow. *Energy Resources Technology-Transactions of the ASME*. 2003; 125: 183-189.
- 659 Smith DC, Elmore AC. The Observed Effects of Changes in Groundwater Flow on a Borehole Heat
660 Exchanger of a Large Scale Ground Coupled Heat pump system. *Geothermics*. 2018; 74: 240-246.
- 661 Shirazi AS, Bernier M. A Small-scale Experimental Apparatus to Study Heat Transfer in the Vicinity of
662 Geothermal Boreholes. *HVAC&R Research*. 2014; 20: 819-827.
- 663 Samson M, Dallaire J, Gosselin L, Gosselin L. Influence of Groundwater Flow on Cost Minimization of
664 Ground Coupled Heat Pump Systems. *Geothermics*. 2018; 73: 100-110.
- 665 Wang H, Qi C. Thermal Performance of Borehole Heat Exchanger under Groundwater Flow: A Case
666 Study from Baoding. *Energy and Buildings*. 2009; 41: 1368-1373.
- 667 Zhang G, Guo Y, Zhou Y. Experimental Study on the Thermal Performance of Tunnel Lining GHE
668 under Groundwater Flow. *Applied Thermal Engineering*. 2016; 106: 784-795.
- 669 Zhang L, Zhao L, Yang L, et al. Analyses on Soil Temperature Response to Intermittent Heat Rejection
670 from BHEs in Soils with Groundwater Advection. *Energy and Buildings*. 2015; 107: 355–365.
- 671 Zhang W, Yang H, Lu L, et al. The Research on Ring-coil Heat Transfer Models of Pile Foundation
672 Ground Heat Exchangers in the Case of Groundwater Seepage. *Energy and Buildings*. 2014; 71:
673 115-128.
- 674 Zhou Z. Spatial Variability and its Effect Mechanism of Soil Salinity in the Low Plain Around the Bohai
675 Sea. Doctoral Dissertation, Chinese Academy of Geological Sciences. Beijing, China, 2012. (in
676 Chinese)
- 677 Østergaard PA, Duic N, Noorollahi Y, et al. Sustainable Development Using Renewable Energy
678 Technology. *Renewable Energy*. 2019; 146: 2430-2437.
- 679

Nomenclature		Λ	tensor of thermal hydrodynamic dispersion($W \cdot m^{-1} \cdot K^{-1}$)
r	distance to the source /sink(m)	δ_{ij}	Kronecker tensor ($i=j, \delta_{ij} =1; i \neq j, \delta_{ij} =0;$)
t	time(s)	γ	compressibility coefficient
l	tube pitch of each BHE(m)	λ	thermal conductivity ($W \cdot m^{-1} \cdot K^{-1}$)

q	heat transfer rates per unit borehole depth of the BHEs ($\text{W}\cdot\text{m}^{-1}$)	α_L, α_T	longitudinal and transverse thermal dispersivity, respectively, of fluid (m)
H	borehole depth(m)	ρc	volumetric heat capacity ($\text{J}\cdot\text{m}^{-3}\cdot\text{K}^{-1}$)
T	temperature (K)	θ	dimensionless temperature
k	permeability(m^2)	Subscripts	
g	gravitational acceleration	x, y	longitudinal and transverse direction, respectively
Q_p	flow intensity of source (sink) term of flow field ($\text{m}^3\cdot\text{m}^{-3}\cdot\text{s}^{-1}$)	r	refrigerant fluid
Q_T	heat intensity of heat source (sink) ($\text{W}\cdot\text{m}^{-3}$)	s	soil
x, y, z	Cartesian coordinates	f	fluid
u	absolute Darcy velocity($\text{m}\cdot\text{s}^{-1}$)	s_0	initial state of rock soil layer
L	dimensionless distance	m	experimental system model
\bar{E}	the average heat transfer efficiency coefficient	i, o	pipe-in or internal, pipe-out or outer, respectively
\bar{Q}	actual average heat exchange quantity (J)	Superscripts	
\bar{Q}'	theoretical average heat exchange quantity (J)	cond	conduction
M	circulating flow flux of refrigerant ($\text{m}^3\cdot\text{s}^{-1}$)	disp	dispersion
Greek symbols			
μ	dynamic viscosity (Pa·s)		
ε	porosity		

680



© 2020 by the authors. Submitted for possible open access publication under the terms and conditions of the Creative Commons Attribution (CC BY) license (<http://creativecommons.org/licenses/by/4.0/>).

681